ARTICLES
https://doi.org/10.1038/s41557-018-0019-6
nature chemistry

An artificial interphase enables reversible magnesium chemistry in carbonate electrolytes

Seoung-Bum Son[1], Tao Gao[2], Steve P. Harvey[1], K. Xerxes Steirer[3], Adam Stokes[1,4], Andrew Norman[1], Chunsheng Wang[2], Arthur Cresce[5], Kang Xu[5] and Chunmei Ban[1*]

Magnesium-based batteries possess potential advantages over their lithium counterparts. However, reversible Mg chemistry requires a thermodynamically stable electrolyte at low potential, which is usually achieved with corrosive components and at the expense of stability against oxidation. In lithium-ion batteries the conflict between the cathodic and anodic stabilities of the electrolytes is resolved by forming an anode interphase that shields the electrolyte from being reduced. This strategy cannot be applied to Mg batteries because divalent Mg^{2+} cannot penetrate such interphases. Here, we engineer an artificial Mg^{2+}-conductive interphase on the Mg anode surface, which successfully decouples the anodic and cathodic requirements for electrolytes and demonstrate highly reversible Mg chemistry in oxidation-resistant electrolytes. The artificial interphase enables the reversible cycling of a Mg/V_2O_5 full-cell in the water-containing, carbonate-based electrolyte. This approach provides a new avenue not only for Mg but also for other multivalent-cation batteries facing the same problems, taking a step towards their use in energy-storage applications.

Rechargeable lithium-ion (Li-ion) batteries based on intercalation chemistries are approaching their energy-density ceiling, so there is an urgent need to explore new battery chemistries that offer high energy density at reduced cost. The rechargeable magnesium metal battery is one such 'beyond Li-ion chemistry', the bivalent nature of which leads to a volumetric capacity (3,832 mAh cm^{-3}) that is nearly twice as high as lithium (2,061 mAh cm^{-3}). This high theoretical value would significantly promote the applications of Mg metal batteries for vehicle electrification and large-scale energy storage[1–5].

Additional enthusiasm for a Mg battery is sparked by the abundance of Mg in the Earth's crust and its non-dendritic nature when crystallizing under electrochemical conditions (in sharp contrast with Li)[6,7]. However, the reversible deposition/stripping chemistry of Mg necessary for operation can only be realized with a solid-state electrolyte that provides a wide voltage window but is kinetically slow[8–10], or when highly corrosive and oxidation-labile electrolytes are used. The most representative examples include the Mg salts based on carbanion (such as Grignard reagents) and hydride anions (such as boron-cluster hydrides) dissolved in ethereal solvents[1–4,11–15]. Unlike the working mechanism for current Li-ion electrodes (in which the reduction of the electrolyte leads to the formation of a Li^+-conducting solid-electrolyte interphase), these exotic electrolyte components do not form passivating layers on Mg anodes, so that Mg deposition/stripping can occur reversibly to enable the cell chemistry[16,17]. These electrolyte components, which are strongly reduction-resistant but oxidation vulnerable and highly corrosive[3,4,14,18–21], basically constitute an intrinsic barrier to the possibility of a high-voltage Mg battery operating above 3.0 V (ref. [17]).

In this work, we report that an artificial Mg^{2+}-conducting interphase can be engineered on the Mg anode surface, which facilitates a reversible Mg deposition/stripping process. More importantly, the low electronic conductivity of this artificial interphase prevents the electrochemical reduction of the electrolyte, thus allowing the use of carbonate solvent that is more resistant to oxidation. The Mg anode protected by such an interphase demonstrated markedly improved performance in both symmetric Mg cells and full Mg/V_2O_5 batteries using non-corrosive Mg salts ($Mg(TFSI)_2$) and carbonate solvent. Furthermore, by using the interphase-protected Mg electrode, we have demonstrated reversible cycling of the Mg/V_2O_5 full cell in an electrolyte containing 3 M water. High intercalation capacity in the V_2O_5 cathode has been known to be achieved by the presence of a small amount of water; however, water would also passivate the Mg surface and eventually shut down the reversible Mg chemistry[22,23]. Only under the protection of an artificial solid-electrolyte interphase (SEI) can reversible Mg plating/stripping at the anode and intercalation/de-intercalation at the cathode be made simultaneously possible in the presence of water. As a proof of concept, we demonstrated that, using this artificial Mg^{2+}-conducting interphase, it is possible to decouple the anodic and cathodic requirements for a Mg electrolyte so that it can support both Mg deposition/stripping at the anode and high-potential intercalations of Mg^{2+} at the cathode. This discovery will provide a new avenue not only for Mg electrolyte design and synthesis that could eventually lead to a high-voltage (>3.0 V) Mg battery, but also in a broader sense for all multi-valent chemistries that faces the same conflicting requirements at anode and cathode surfaces.

Results and discussion

Characterization of the artificial Mg^{2+}-conducting interphase. The artificial interphase is a Mg^{2+}-conducting polymeric film made from thermal-cyclized polyacrylonitrile (cPAN with a molecular formula of $(C_3H_3N)_n$) and Mg trifluoromethanesulfonate ($Mg(CF_3SO_3)_2$), also known as Mg triflate. The detailed protocol for synthesizing this interphase is described in the Methods section. Under high-resolution transmission electron microscopy

[1]National Renewable Energy Laboratory, Golden, CO, USA. [2]Department of Chemical and Biomolecular Engineering, University of Maryland, College Park, MD, USA. [3]Department of Physics, Colorado School of Mines, Golden, CO, USA. [4]Department of Materials Science, Colorado School of Mines, Golden, CO, USA. [5]Electrochemistry Branch, Sensor and Electron Devices Directorate, US Army Research Laboratory, Adelphi, MD, USA. *e-mail: chunmei.ban@nrel.gov

(HRTEM), the pristine polymeric coating appears to be a film with a thickness of about 100 nm, as shown in Fig. 1a. Further microstructure observations were performed with scanning transmission electron microscopy (STEM) high-angle annular dark-field (HAADF, Fig. 1b) mode and STEM energy-dispersive X-ray spectroscopy (EDS, Fig. 1c–h) mapping; the STEM-HAADF image shows the compositional difference between the artificial interphase and Mg particles. EDS elemental mapping (C, N, Mg, F, O) across the selected area of the artificial Mg^{2+} conductive interphase reflects the distribution of Mg^{2+} and ($CF_3SO_3^-$) anions in the cPAN matrix. The EDS spectrum of the corresponding STEM EDS mapping area is shown in Supplementary Fig. 1.

Annealing treatment of the pristine composite coating is critical in converting it into a functional polymeric interphase. This process was believed to be responsible for triggering the thermal cyclization of PAN units[24]. The products of this cyclization, cPAN, include pyridine-based aromatic rings and have been proven to mitigate continuous volume changes of active materials upon lithiation, which is a vital characteristic for surface modification of battery electrode materials[25,26]. X-ray photoelectron spectroscopy (XPS) of the N 1*s* core level in Fig. 2 depicts the structural evolution of this polymeric interphase induced by annealing. The nitrile group (N1, C≡N, at 400.4 eV) present in the pristine PAN matrix was found to gradually transform to a mixture of pyridinic (N2, C–N=C, at 398.8 eV) and substitutional graphite species (N3, N coordinated with three C atoms, at 399.8 eV) upon cyclization[24,27,28]. Quantitative analysis reveals that 69.25% of substitutional graphite species and 30.75% of the pyridinic structure was achieved after thermal cyclization. Such an elastic polymeric component should accommodate the drastic volumetric changes during reversible Mg deposition/stripping reactions[25].

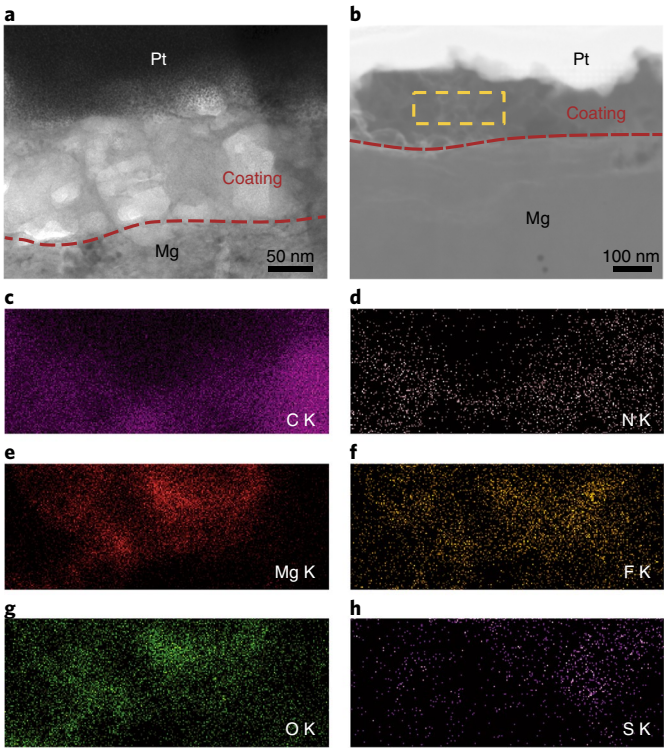

Fig. 1 | TEM imaging and EDS mapping of the artificial Mg^{2+}-conducting interphase. a, The coated Mg metal with the artificial Mg^{2+}-conducting interphase. Conformal coating thickness of 100 nm is observed on the Mg surface. **b**, STEM HAADF mode observation of Mg metal with the Mg^{2+}-conductive coating layer. STEM EDS mapping area is indicated by the yellow rectangular box. **c**–**h**, EDS mapping of C (**c**), N (**d**), Mg (**e**), F (**f**), O (**g**) and S (**h**) in the coating.

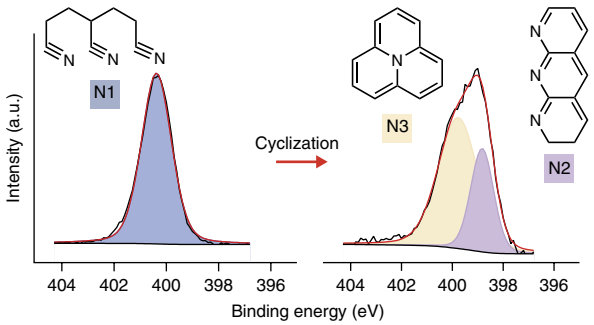

Fig. 2 | XPS analysis of Mg^{2+}-conducting film. The shift in the binding energy in N 1s core shows a structural change of the nitrile group (N1) to pyridinic (N2) and substitutional graphite group (N3) after cyclization. The raw spectrum is shown as black and the fitted line is shown as red.

Reversible Mg chemistry in reduction-vulnerable electrolytes. The reversibility of Mg deposition and stripping was tested in three electrolytes using a symmetric cell configuration consisting of two identical Mg electrodes. One electrolyte is the well-established but highly corrosive and oxidation-vulnerable Grignard electrolyte APC (all phenyl complex, or $(PhMgCl)_2$-$AlCl_3$/THF) (ref. [20]). Two other electrolytes are based on stable Mg salts (0.5 M $Mg(TFSI)_2$) dissolved in acetonitrile (ACN) and propylene carbonate (PC)[29]. In particular, the carbonate ester is non-corrosive, highly resistant to oxidation[30,31] and has been extensively explored in Li-ion battery research; but it cannot support the reversible Mg deposition/stripping chemistry due to its reductive decompositions on the Mg surface, leading to the formation of a semi-carbonate interphase with negligible Mg^{2+} conductivity[11]. The deposition/stripping process was set with half-hour or one-hour intervals at a cycling rate of 0.01 mA cm^{-2} and a voltage limit of 2 V for APC and ACN, or 3 V for PC.

As shown in Fig. 3a, in APC electrolyte, reversible deposition/stripping reactions were observed for both uncoated and coated Mg electrodes. Slightly higher plating overpotential (~0.1 V) was observed for the coated Mg electrodes in the first 100 h as compared with the uncoated Mg electrodes; this difference is due to the lower Mg^{2+} conductivity in the artificial interphase than that in the APC electrolyte. The overpotential gradually decreased to the same level as the uncoated Mg electrode. It is expected that the interphase experiences an activation process in APC electrolyte. Cyclic voltammetry of both uncoated and coated Mg electrodes is presented in Supplementary Figs. 2 and 3.

However, when the electrolyte was switched to reduction-vulnerable electrolytes such as 0.5 M $Mg(TFSI)_2$ dissolved in either ACN (as shown in Supplementary Fig. 4) or PC (Fig. 3b), the uncoated Mg electrode experienced extremely high and rapidly increased overpotential (>1.0 V) with cycles, which is apparently caused by the Mg-surface passivation as a result of reductions of ACN and PC. This passivation quickly shuts off the passage of Mg^{2+}, as indicated by the irreversible deposition/stripping behaviour and the rapidly rising impedance. In sharp contrast, the coated Mg electrode in PC-based electrolyte exhibits better reversibility for 1,000 h without pronounced overpotential build-up during the extended cycles (Fig. 3b,c). Additionally, Supplementary Fig. 5 plots the voltage hysteresis—the difference between the voltages of Mg stripping and plating—as a function of current density, to demonstrate the rate performance of the coated Mg electrode in the PC-based electrolyte. The artificial interphase enables the reversible Mg chemistry for the coated Mg metal electrodes even in the carbonate-based electrolyte, in contrast to no reactivity observed for the untreated Mg metal. Although an increase in the voltage hysteresis is observed at the higher current densities, all of the cells exhibit sustainable Mg

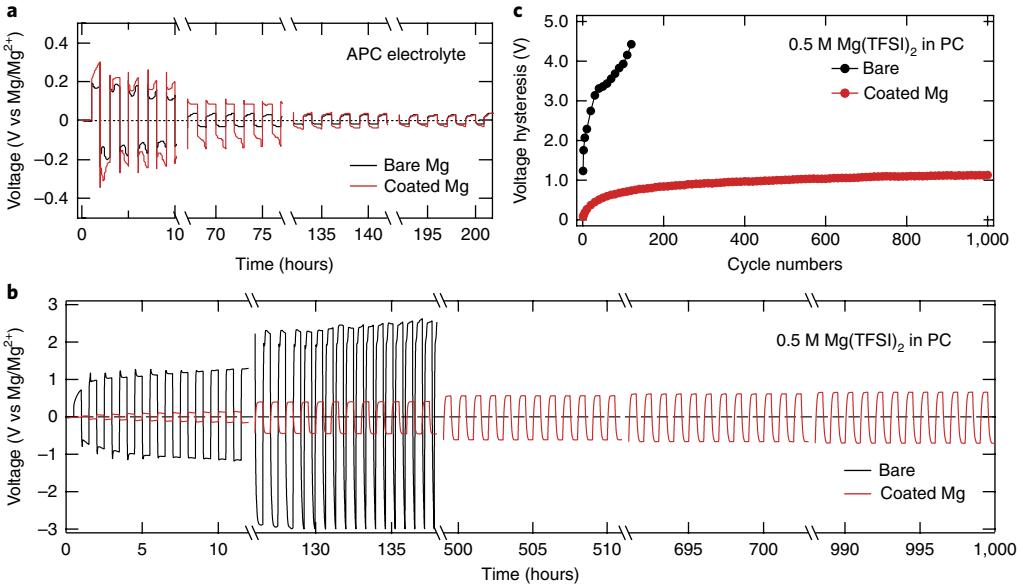

Fig. 3 | Voltage responses of symmetric Mg cells under repeated polarization with and without artificial interphase in different electrolyte systems at a current density of 0.01 mA cm^{-2}. a,**b**, Reversible Mg deposition/stripping in APC electrolyte (**a**), where each deposition/stripping cycle lasts for an hour, and in 0.5 M Mg(TFSI)$_2$/PC electrolyte (**b**), where each deposition/stripping cycle lasts for a half hour. The cell made with pristine Mg electrodes shows huge overpotential at the beginning and fails after 135 cycles, whereas the cell made with the Mg^{2+}-conducting interphase-protected Mg electrodes performs prolonged cycles in carbonate-based electrolytes. The reversibility is conspicuous in the latter as proven by up to 1,000 cycles. **c**, Voltage hysteresis versus cycle numbers for symmetric Mg electrodes with 0.5 M Mg(TFSI)$_2$/PC electrolyte. Lower voltage hysteresis is observed on interphase-protected Mg electrode, where reductive decomposition of PC is prevented because of the artificial interphase.

deposition/stripping. Furthermore, the surface morphology of the coated Mg anode exhibits negligible changes before and after electrochemical cycling, as shown in Supplementary Fig. 6.

The failure of the uncoated Mg electrode in nitrile or carbonate electrolytes presents no surprise based on the established knowledge that non-conductive interphases were formed by the reductive decompositions of these electrolytes. However, what surprises us is that the artificial Mg^{2+}-conducting interphase enables the highly reversible Mg deposition/stripping process in those electrolytes. Such an interphase seems to prevent the Mg from direct chemical reaction with ACN and PC at the Mg-ion deposition potential, while it still allows the passage of Mg^{2+} ions. The reversible Mg plating/stripping chemistry has only been achieved in the thermal-treated Mg electrode (as shown in Supplementary Fig. 7), indicating the necessity of the thermal-cyclization process for forming the Mg^{2+}-conducting interphase.

In fact, this is the first time that a carbonate-based electrolyte, which is well-known in Li-ion chemistries for its high stability against oxidation[31,32], is shown to support reversible Mg deposition/stripping chemistry. Upon closer examination, the voltage hysteresis clearly reveals that the polymeric interphase significantly reduced the overpotentials for Mg deposition/stripping chemistry in PC-based electrolyte. It appears that the artificial polymeric interphase not only successfully prevents the reduction of these reduction-vulnerable solvents, but also promotes the Mg^{2+} transport.

Chemical structure analysis of the artificial interphase. Further analysis on the structure of the polymeric interphase was conducted with time-of-flight secondary-ion mass spectrometry (TOF-SIMS), with measurements collected from cPAN-based polymeric interphase with and without $Mg(CF_3SO_3)_2$ and plotted together in Fig. 4a–c. A signal corresponding to the positive secondary-ion Mg^+, which was generated by the interaction of Mg^{2+} with the analysis beam, appears at $m/z = 24$ only with cPAN with $Mg(CF_3SO_3)_2$, which indicates that $Mg(CF_3SO_3)_2$ is the main source of Mg^+. Meanwhile, Mg^+ was also detected at much lower abundance in cPAN containing no $Mg(CF_3SO_3)_2$, because of the Mg substrate beneath the interphase (Fig. 4a). In addition to the Mg^+ ions, the negative ions $CF_3SO_3^-$ and $[Mg(CF_3SO_3)_3]^-$ are also most pronounced in the artificial interphase, as shown in Fig. 4b,c. Collectively, these observations indicate that Mg ions are multi-coordinated with $CF_3SO_3^-$ anions, and a polymeric networking of $CF_3SO_3^-$ and $[Mg(CF_3SO_3)_3]^-$ has probably formed throughout the Mg^{2+}-conducting layer[33]. Therefore, we speculated that structurally, the polymeric interphase contains a pyridine-based PAN matrix hybridized with a network of multi-coordinated $Mg(CF_3SO_3^-)$ units, as illustrated in Fig. 4e. This network facilitates the release of Mg^{2+} from its solvation cage and its diffusion through the film. Thermogravimetric analysis (Fig. 4d) compares the stabilities of $Mg(CF_3SO_3)_2$, PAN, and PAN-$Mg(CF_3SO_3)_2$ upon heating. PAN experiences an early and sluggish process of weight loss below 200 °C, whereas the thermal decomposition of $Mg(CF_3SO_3)_2$ shows a sudden onset at 400 °C, losing ~81 wt% of its original mass in a narrow range of 40 °C. However, the complex of the two, PAN-$Mg(CF_3SO_3)_2$, does not follow either; rather, it adopts a unique profile that combines characteristics of both, which very probably indicates the coupling between the two components via ion-dipole interaction, forming the multi-coordinated $Mg(CF_3SO_3^-)$ units in the Mg^{2+}-conducting layer. This polymeric network of multi-coordinated $Mg(CF_3SO_3^-)$ units inhibits the interaction between the artificial interphase and the liquid electrolyte through both physical and chemical barriers. During the cell reaction, Mg^{2+} can diffuse across this Mg^{2+}-conducting interphase, but it can be difficult for the large $TFSI^-$ anion in the electrolyte to pass through this Mg^{2+}-conducting layer filled with multi-coordinated $[Mg(CF_3SO_3)_3]^-$ anions.

Conductivity of the artificial interphase. The ionic conductivity of the artificial interphase was measured at room temperature by electrochemical impedance spectroscopy (EIS). The configuration of the cell and the details of measurement method are shown in Supplementary Fig. 8, and the typical Nyquist plot is presented in Fig. 5a. An average ionic conductivity of 1.19×10^{-6} S cm^{-1} was achieved according to

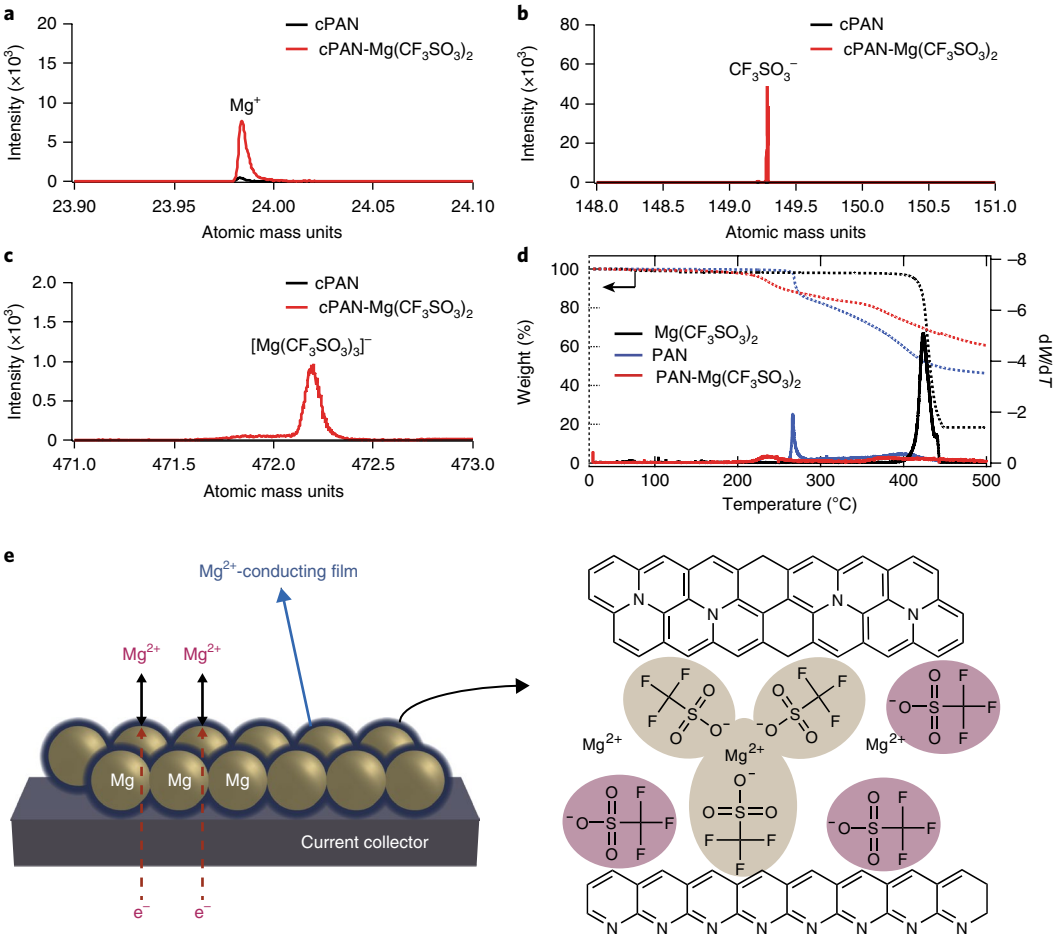

Fig. 4 | TOF-SIMS and TGA analysis of Mg^{2+}-conducting interphase. a–c, TOF-SIMS spectra for positive Mg ions from the cyclized PAN film and the Mg^{2+}-conducting film made of cPAN and $Mg(CF_3SO_3)_2$ (labelled as cPAN-$Mg(CF_3SO_3)_2$) (**a**), and for negative ions from the cyclized PAN film and the Mg^{2+}-conducting film (**b**,**c**). Both signals for $CF_3SO_3^-$ and $[Mg(CF_3SO_3)_3]^-$ are only pronounced for the Mg^{2+}-conducting film. **d**, TGA analysis of $Mg(CF_3SO_3)_2$, PAN and the film made of PAN and $Mg(CF_3SO_3)_2$. Weight losses (wt%) versus temperature (°C) for $Mg(CF_3SO_3)_2$, PAN, and the film made of PAN and $Mg(CF_3SO_3)_2$ are shown as dashed lines. TGA was performed under nitrogen at a ramping rate of 1 °C per minute to 500 °C. In differentiated plots (solid lines), each peak indicates where thermal decompositions of the samples occur. **e**, Schematic of a Mg powder electrode coated with the artificial Mg^{2+}-conducting interphase, and the proposed structure for the artificial Mg^{2+}-conducting interphase based on XPS, TOF-SIMS and TGA analysis.

results collected from three independent cells. This value is comparable to the ion conductivities known for Li^+-polymer electrolytes[34], but is much higher than that estimated for a typical SEI in a Li-ion battery consisting of semi-carbonate salt (10^{-9} S cm^{-1})[30]. In the electrochemical cell, the artificial interphase with the high ionic conductivity of 1.19×10^{-6} S cm^{-1} has a thickness of about 100 nm, which allows transporting Mg^{2+} at high rates. This artificial interphase is surprisingly conductive considering that divalent ions are always less mobile than their single-valent counterparts due to the much higher Coulombic drag. Combined with mechanical strength, this polymeric interphase ensures facile Mg^{2+} transport while accommodating the reversible Mg deposition/stripping process.

The electronic conductivity of the Mg^{2+}-conducting film was evaluated at room temperature using two separate methods—a direct-current polarization technique[35] and linear-scan voltammetry (LSV)[36]. Figure 5b shows the linear-sweep voltammogram as a function of voltage at a low scan rate of 1 mV s^{-1}. A linear curve is clearly identified and the slope of the voltage–current curve was used to calculate the electronic resistance. The electronic conductivity calculated from both methods is within the same order of magnitude. Note that the electronic conductivity is only about 1.04×10^{-7} S cm^{-1} as plotted in Fig. 5b, which is ten times lower than the ionic conductivity. The low electronic conductivity is attributed to the presence of a conjugated sp^2 carbon network formed in the thermal-cyclized PAN. Due to the low electronic conductivity of the artificial interphase, no electron crossover is expected, precluding the deposition of Mg metal on top of the interphase and reduction of electrolytes on the top surface of thermal-cyclized PAN. As indicated in Supplementary Fig. 9, the absence of Mg deposition and electrolyte reduction on top of the interphase was confirmed by TEM images collected after deposition; and the artificial Mg-ion SEI is preserved after intensive electrochemical cycling. Summarizing the above results, this is the first-known Mg^{2+}-conducting artificial SEI to the best of our knowledge.

Depth analysis of the cycled Mg electrode. To confirm that Mg is indeed deposited in the solvents, we performed depth profiling using X-ray photoelectron spectroscopy (XPS) combined with scanning electron microscopy (SEM)-EDS on the uncoated and coated electrodes after electrochemical deposition. The voltage profile is plotted in Supplementary Fig. 10. SEM-EDS data confirm that Mg deposition is only achieved with the coated stainless steel (SS) electrode, as displayed in Supplementary Figs. 11 and 12. XPS depth profiling, by combining ion gun etch cycles interleaved with XPS measurements, was also used to provide the composition along the thickness of the coated electrode. Figure 5c depicts the intensity evolution for Mg, C, Fe, N and O components in the coated electrode,

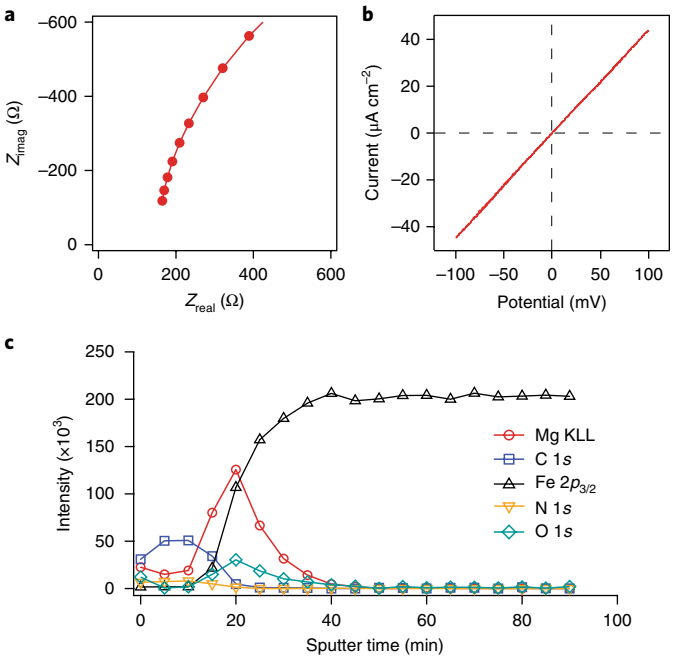

Fig. 5 | Conductivity measurement of Mg^{2+}-conducting interphase on Mg surface and XPS depth profiles. a, Nyquist plot for ionic conductivity measurement of the Mg^{2+}-conducting film. Conductivity cells consisting of Mg^{2+}-conducting film sandwiched between two stainless-steel disks, which act as ion-blocking electrodes, were prepared. **b**, A linear-sweep voltammogram of the above cell at 1 mV s^{-1} scan rate within −0.1 V to +0.1 V. **c**, XPS depth-profiles of the coated stainless-steel electrode in the 0.5 M $Mg(TFSI)_2$-PC electrolyte.

as a function of the sputtering time. Unfortunately, atomic percentages were not included in the plots because the presence of Fe 3*s* and Fe 3*p* overlaps with the Mg 2*s* and 2*p* peak. Therefore, the Mg KLL auger peak rather than Mg 2*s* was used here to identify the presence of Mg metal. On the basis of the XPS depth-profile, two distinct layers cover the surface of the electrode. The upper layer consists of the Mg $^{2+}$-conductive film, as indicated by the intensity of C and N and the absence of Fe. The lower layer consists of the Mg deposition layer. Mg is present through the conductive film, but its concentration increases significantly at the surface of the SS electrode. The Mg signal drops off rapidly as the sample becomes increasingly Fe-rich. Some adventitious O is noted on the initial surface scan prior to sputtering. The presence of oxygen is expected because of air contamination during sample preparation and transportation. The low content of nitrogen observed for XPS (not identified in the EDS) is consistent with the compositional analysis of the conductive interphase. XPS depth profiling combined with the results from SEM-EDS clearly confirm that the conductive film facilitates the diffusion of Mg ions through the conductive interphase and enables Mg deposition on the surface of the electrode.

Full cell demonstration in the PC– and PC+ H_2O-based electrolytes. A full prototype cell was assembled to prove the robustness of an artificial Mg^{2+}-conducting interphase. An orthorhombic V_2O_5 cathode, which is a well-established intercalation cathode for Li^+ (ref. [37–40]) (Supplementary Fig. 13), was coupled with a Mg metal anode with or without the conductive interphase. The cells were charged/discharged in the 0.5 M $Mg(TFSI)_2$/PC electrolyte at a rate of 29.4 mA g^{-1}. The electrochemical results are summarized in Fig. 6a,c. As displayed in Fig. 6a, we observed significantly improved reversibility and cycling stability in the PC-based electrolyte when the interphase-protected Mg anode was used. Low capacity utilization was observed due to the large particle size and non-optimized cathode composition; nevertheless, we demonstrated a successful proof of concept here with the sustainable cycling performance, which is achieved for the first time in a carbonate-based electrolyte. As a comparison, when the Mg surface is not protected by such an interphase, we observed rapid capacity fading accompanied with a sharp rise in overpotential (Fig. 6a,c). During the first magnesiation process, both Mg electrodes deliver ~70 mAh g^{-1} (71 mAh g^{-1} for the bare-Mg electrode and 76 mAh g^{-1} for the protected Mg electrode), which corresponds to about 0.24 moles of Mg ions intercalated into one mole of V_2O_5. However, the capacity of the bare-Mg/V_2O_5 full cell drops rapidly to zero after 40 cycles. The severe capacity decay on the cell made with the pristine Mg anode is apparently caused by the formation of an ad hoc interphase from the reduction of PC, which insulates Mg^{2+} from migration; on the other hand, a sustainable cycling performance with a reversible capacity of 47 mAh g^{-1} is achieved over 40 electrochemical cycles by using the interface-protected Mg anode coated with this artificial Mg^{2+}-conductive interphase. X-ray diffraction (XRD) measurements provide structural evidence for the repeated intercalation/de-intercalation chemistry of Mg^{2+} ions in the lattice of V_2O_5, where the main (200) and (110) peaks are shifted to the lower 2θ values after initial magnesiation and recovered to their original positions after demagnesiation (Fig. 6d). Apparently, a new phase that was formed during magnesiation disappears during demagnesiation, and this mechanism needs further investigation.

It has been reported that adding 0.5–1.0 M H_2O into $Mg(ClO_4)$/ACN organic electrolyte can significantly increase the capacity of V_2O_5 from 50 mAh g^{-1} to 100 mAh g^{-1} because the H_2O can co-insert into V_2O_5 with Mg^{2+}, which significantly accelerates the Mg^{2+} insertion kinetics[23,41]. However, trace water in organic electrolyte will seriously damage the reversibility of Mg anodes, limiting its practical use in Mg/V_2O_5 full cells. Earlier, it was predicted that the surface protection was necessary to enable reversible Mg chemistry in the water-containing electrolyte[42]. Because the artificial interphase in this work can prevent the reactions of electrolytes with a Mg electrode, we believe that it would also act as a barrier to the reaction between Mg and water, making the water effect on accelerated kinetics of V_2O_5 practical. To demonstrate the stability and effectiveness of the artificial interphase against water, 3 M water was added to the PC-based electrolyte (0.5 M $Mg(TFSI)_2$/PC). A rapid capacity decay to zero within eight cycles is observed for the Mg/V_2O_5 cell in 0.5 M $Mg(TFSI)_2$/PC + 3 M H_2O electrolyte with the pristine Mg metal anode (Fig. 6b,c). However, with the artificial Mg^{2+}-conductive interphase on Mg metal anode, the reversible capacity of the coated Mg/V_2O_5 full cell showed a pronounced increase to 140 mAh g^{-1} after the fifth cycle, in conjunction with a decreased overpotential value. The reversible capacity of 140 mAh g^{-1} is comparable to those of LiV_2O_5 and $LiCoO_2$, which can insert about 0.5 Li per transitional metal without irreversible phase changes. The V_2O_5 cathode could have a theoretical capacity of ~294 mAh g^{-1} for a two-electron reaction (for example, MgV_2O_5), if using a wide operating voltage window[43]. In our study, the cell was cycled between 0.5 V and 2.5 V, to facilitate an one-electron reaction[44]. The full cell Mg/V_2O_5 battery delivers about 140 mAh g^{-1}, which is very close to the theoretical capacity for an one-electron reaction (~147 mAh g^{-1}, for example, $Mg_{0.5}V_2O_5$) (ref. [44]). Supplementary Fig. 14 provides detailed electrochemical performances of coated Mg against V_2O_5 including coulombic efficiency (CE). No major morphological differences were observed for the coated Mg anode at the different electrochemical states, as indicated in Supplementary Fig. 15.

The enhancement in Mg^{2+} intercalation with increased operating potential is due to both reduced desolvation energy for hydrated Mg^{2+} and suppressed Coulombic repulsion between Mg^{2+} ions and the host surface[22,41,42,45]. On the anode side, the artificial

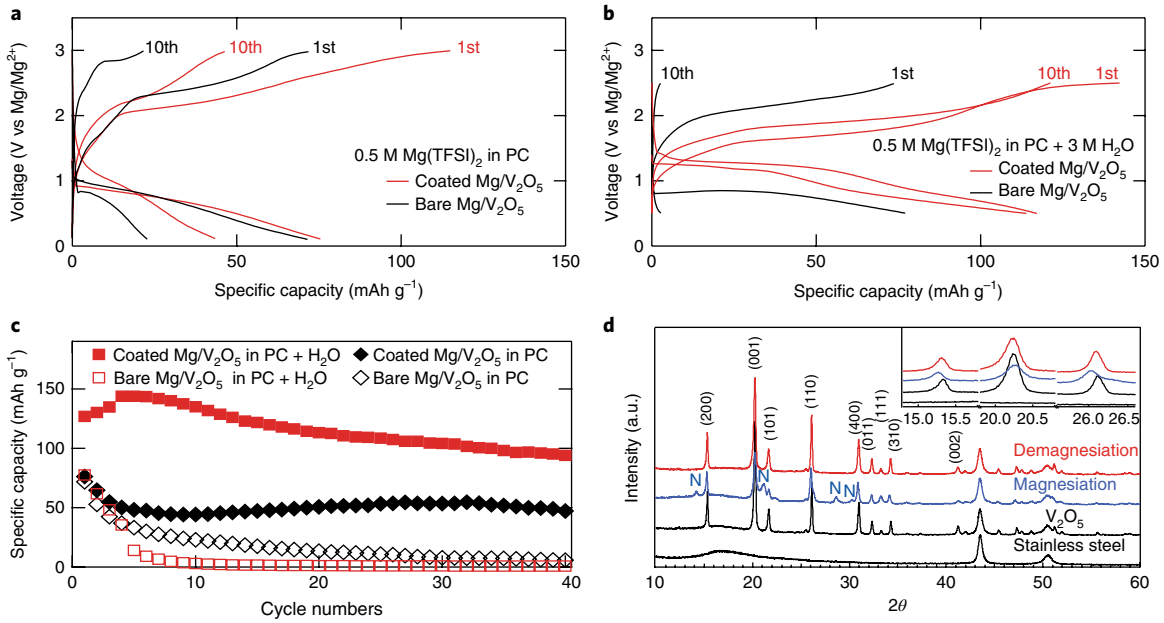

Fig. 6 | Electrochemical performance of the Mg/V_2O_5 full cell. a, Voltage profiles of full cells using a bare Mg anode (black lines) and an interphase-protected Mg anode (red lines) between 0.01 and 3 V at a current density of 29.4 mA g^{-1}; 0.5 M $Mg(TFSI)_2$/PC electrolyte was used here. Voltage profiles of the first and tenth cycle are presented for both cells. The bare Mg/V_2O_5 cell shows rapid capacity losses during cycling, whereas interphase-protected Mg/V_2O_5 shows stable capacity retention. **b**, Voltage profiles of full cells using a bare Mg anode (black lines) and an interphase-protected Mg anode (red lines) between 0.5 and 2.5 V at a current density of 29.4 mA g^{-1} with water-containing electrolyte (0.5 M $Mg(TFSI)_2$/PC + 3 M H_2O electrolyte). Voltage profiles of the first and tenth cycle are presented for both cells. **c**, Full-cell cycling performance comparisons between Mg/V_2O_5 and Mg (interphase-protected)/V_2O_5 in 0.5 M $Mg(TFSI)_2$/PC electrolyte and 0.5 M $Mg(TFSI)_2$/PC + 3 M H_2O electrolyte. Surface modification of Mg electrode with Mg^{2+}-conducting interphase remarkably improves cycling stability in both nonaqueous carbonate electrolyte and water-containing electrolyte. **d**, XRD analyses of pristine, magnesiated and demagnesiated V_2O_5 (matched with JCPDS 41-1426). Inset of **d** magnifies peaks of (200) and (110) that shift to lower two-theta degrees when magnesiated and recover after demagnesiation. Peaks appearing after magnesiation are denoted as N and diminished after demagnesiation.

interphase clearly segregated the Mg anode from any irreversible reaction with water in the electrolyte. Most importantly, the artificial interphase suppresses the electrochemical decompositions of the water-containing carbonate-based electrolyte and ensures the reversible electrochemical performance in the full cell. By using the interface-protected Mg anode, we are able to provide the first direct demonstration of using the water-containing electrolyte in a full cell including a Mg metal anode and a V_2O_5 cathode. The successful demonstration implies the feasibility of using an artificial Mg^{2+}-conductive interphase to facilitate Mg^{2+} diffusion without passivating Mg metal. Additionally, the artificial SEI layer on Mg allows the use of an oxidation-resistant electrolyte such as carbonate-based solvents, and it will provide great opportunities to explore high-voltage operating cathode materials for a high-energy Mg battery system.

Conclusions

In summary, we have reported a new approach to resolve the dilemma faced in the Mg battery, that is, the conflict between an ethereal organometallic electrolyte and the desired oxidation stability, by engineering an artificial Mg^{2+}-conductive interphase on the surface of a Mg metal electrode, so that reversible Mg plating/stripping chemistry can be enabled in high-voltage electrolytes known to be troublesome for Mg batteries. The elastic and Mg^{2+}-conducting but electronic-insulating polymeric interphase on the surface of Mg metal can effectively prevent the electrochemical reduction of the electrolytes and the water therein, while still allowing Mg^{2+} to migrate (ionic conductivity 1.19×10^{-6} S cm^{-1}), thus making it possible to use electrolyte components that are oxidation-resistant and non-corrosive. Superior performances of full cells using the interphase-protected Mg electrodes have demonstrated the feasibility of constructing high-energy Mg-metal batteries with high-voltage oxide cathodes and oxidation-resistant electrolytes; such characteristics have been precluded by the conventional approach of ethereal-based Mg electrolytes. Above all, the compatibility of the artificial SEI-protected Mg anode with water has been well verified in a full-cell test, rendering it feasible to construct a rechargeable magnesium battery with both fast kinetics and better reversibility. In the past two decades, many researchers have pointed out that water co-intercalation can dramatically enhance the intrinsically slow Mg^{2+} intercalation kinetics[42,46]. For these reasons, using the artificial interphase approach on a Mg anode provides an unprecedented avenue for simultaneously addressing the anode/electrolyte incompatibility and cathode kinetics limitation, leading to novel high-energy/high-power rechargeable Mg batteries.

Methods

Fabrication of Mg electrodes. The Mg electrode with an artificial interphase was composed of Mg powder (Alfa Aesar, –325 mesh), carbon black, PAN and $Mg(CF_3SO_3)_2$ in a weight ratio of 77:10:10:3. The presence of the native oxide layer is the intrinsic characteristic of the Mg metal. It is difficult to remove the native oxide layer, due to the reactivity of the pure Mg metal and the stability of the magnesium oxide. In our study, we did not treat the as-received Mg particles. The prepared mixture was dissolved in dimethylformamide (DMF) and stirred using a magnetic bar for 5 h. The Mg electrode was prepared by casting the obtained slurry on SS foil. The coated electrode was annealed at 300 °C for 1 h under Ar to trigger the cyclization of PAN units. The bare Mg electrode comprised 80% Mg, 10% carbon black and 10% polyvinylidene fluoride (PVDF) binder. The slurry in *N*-methylpyrrolidone (NMP, Sigma Aldrich) was thoroughly mixed before coating. An applicator was used to blade the slurries onto SS current collectors. All handling of Mg electrodes was conducted in a glove box filled with Ar. All Mg electrodes were punched in the diameter of 15 mm (1.766 cm^2) for the electrochemical tests.

Electrochemical test. Materials were evaluated electrochemically in 2,032 coin cells. Biologic and Arbin electrochemical stations were used for both cyclic

voltammetry and galvanostatic cycling measurements. All electrochemical testing was conducted at room temperature.

Preparation of V_2O_5 electrode. The V_2O_5 cathode was prepared using microsized particles purchased from Aldrich. Three grams of V_2O_5 powders (Alfa Aesar) were ball-milled for 50 h and then heat-treated at 650 °C for 5 min before mixing with the electrode additives[47]. The V_2O_5 electrodes used here comprised 70% V_2O_5 (0.5 mg cm^{-2}), 15% carbon black (CB), and 15% PVDF binder on the SS current collector. The V_2O_5 electrodes were punched in the diameter of 3/8 inch (0.712 cm^2) for the full cell tests.

Microstructure and X-ray diffraction analysis. A focused ion beam (FIB) etching and deposition tool (FEI, Nova 200 Nanolab dual-beam system) was used for TEM sample preparation using a conventional lift-out method. The SEM-EDS was performed with the electron beam condition of 5 kV and 1.6 nA. For the TEM preparation, Pt deposition was applied to protect the surface of the desired observation area with the electron beam to minimize the damage on the coating layer, followed by Ga^+ ion-beam Pt deposition. A 30 kV Ga^+ ion beam was used for FIB sectioning with the final milling performed using a 5 kV Ga^+ ion beam to minimize ion-beam damage. The microstructure of the Mg^{2+}-conducting film was investigated by analytical TEM (FEI Tecnai F20 UT and FEI Talos F200X field-emitting gun (FEG) STEMs equipped with EDS) operating at 200 keV. XRD data for phase determination were collected with an X-ray diffractometer (XRD, Rigaku DMax) with Cu-Kα radiation.

Secondary-ion mass spectrometry measurement. A TOF-SIMS V spectrometer (IONTOF) was used to determine the composition of the artificial interphase before and after the thermal treatment. Surface spectra were acquired using a Bi^{3+} primary-ion beam (operated in bunched mode; 21 ns pulse width, analysis current of 0.6 pA), scanned over a 50 μm × 50 μm area, using a low-energy electron flood gun for charge compensation. A 150 μs cycle time was used, yielding mass spectra with a range of 1 to 2,000 a.m.u. All spectra were collected at a primary ion dose density of 1×10^{12} ions cm^{-2} to remain under the static-SIMS limit.

X-ray photoelectron spectroscopy measurement. Samples were transferred without air exposure to an N_2 atmosphere glove box connected to the XPS system. XPS experiments were performed using a Physical Electronics (PHI) 5600 photoelectron spectrometer. Excitation was provided with a monochromatized Al anode (Kα radiation at 1,486.6 eV) operating at 25 mA and 15 kV. Core-level spectra were collected at analyser pass energy of 11.75 eV. The XPS binding energies were calibrated by comparing centroid positions of clean Cu $2p_{3/2}$, Ag $3d_{5/2}$ and Au $4f_{7/2}$ from measured and accepted values. The spectra were fit and analysed in Multipak software. No charging of the samples was observed.

XPS depth profile. The SS foils (area of 1.766 cm^2) with and without the Mg^{2+}-conductive coating were used as the electrodes to deposit the Mg metal from the 0.5 M $Mg(TFSI)_2$/PC electrolyte, while the Mg metal was used as the counter electrode. Constant current with a current density of 0.01 mA cm^{-2} was applied to the cells for Mg deposition on the uncoated/coated SS electrodes. After the electrochemical Mg deposition, the uncoated and coated electrodes were obtained after disassembling the cells in the Ar-filled glove box, and sent for XPS analysis. XPS was performed on a PHI Versaprobe 3 instrument using a spot size of 100 μm and a spot energy of 25 W. Samples were loaded into a sealed container in an Ar-filled glovebox with moisture content of less than 1 ppm H_2O and an O_2 content of 1 ppm. Samples were then transferred directly to the XPS sample chamber such that they were never exposed to the outside environment. Depth profiles were collected using an Ar-ion sputter time of 5 min with an accelerating potential of 3 kV rastered over an area of approximately 300 μm. A surface profile was collected pre-sputter, then profiles were collected after every 5 min sputtering period.

Thermogravimetric analysis. Thermogravimetric analysis (TGA) was performed using a TA Instruments SDT Q600 Simultaneous TGA/DSC system. Five milligrams of the sample were placed in a platinum crucible and then into the TGA/DSC for analysis. The sample was heated to 500 °C under nitrogen flow at a ramping rate of 1 °C per minute.

Data availability. The data supporting the findings of this study are available within the paper and its Supplementary Information files, and are available from the corresponding author upon reasonable request.

Received: 27 March 2017; Accepted: 1 February 2018;
Published online: 2 April 2018

References

1. Mohtadi, R. & Mizuno, F. Magnesium batteries: current state of the art, issues and future perspectives. *Beilstein. J. Nanotechnol.* **5**, 1291–1311 (2014).
2. Muldoon, J., Bucur, C. B. & Gregory, T. Quest for nonaqueous multivalent secondary batteries: magnesium and beyond. *Chem. Rev.* **114**, 11683–11720 (2014).
3. Aurbach, D., Weissman, I., Gofer, Y. & Levi, E. Nonaqueous magnesium electrochemistry and its application in secondary batteries. *Chem. Rec.* **3**, 61–73 (2003).
4. Aurbach, D. et al. Prototype systems for rechargeable magnesium batteries. *Nature* **407**, 724–727 (2000).
5. Song, J., Sahadeo, E., Noked, M. & Lee, S. B. Mapping the challenges of magnesium battery. *J. Phys. Chem. Lett.* **7**, 1736–1749 (2016).
6. Matsui, M. Study on electrochemically deposited Mg metal. *J. Power Sources* **196**, 7048–7055 (2011).
7. Ling, C., Banerjee, D. & Matsui, M. Study of the electrochemical deposition of Mg in the atomic level: why it prefers the non-dendritic morphology. *Electrochim. Acta* **76**, 270–274 (2012).
8. Aubrey, M. L., Ameloot, R., Wiers, B. M. & Long, J. R. Metal–organic frameworks as solid magnesium electrolytes. *Energ. Environ. Sci.* **7**, 667–671 (2014).
9. Higashi, S., Miwa, K., Aoki, M. & Takechi, K. A novel inorganic solid state ion conductor for rechargeable Mg batteries. *Chem. Commun.* **50**, 1320–1322 (2014).
10. Pandey, G. P., Agrawal, R. C. & Hashmi, S. A. Magnesium ion-conducting gel polymer electrolytes dispersed with fumed silica for rechargeable magnesium battery application. *J. Solid State Electr.* **15**, 2253–2264 (2011).
11. Lu, Z., Schechter, A., Moshkovich, M. & Aurbach, D. On the electrochemical behavior of magnesium electrodes in polar aprotic electrolyte solutions. *J. Electroanal. Chem.* **466**, 203–217 (1999).
12. Yoo, H. D. et al. Mg rechargeable batteries: an on-going challenge. *Energ. Environ. Sci.* **6**, 2265–2279 (2013).
13. Muldoon, J. et al. Electrolyte roadblocks to a magnesium rechargeable battery. *Energ. Environ. Sci.* **5**, 5941–5950 (2012).
14. Liebenow, C., Yang, Z. & Lobitz, P. The electrodeposition of magnesium using solutions of organomagnesium halides, amidomagnesium halides and magnesium organoborates. *Electrochem. Commun.* **2**, 641–645 (2000).
15. Mohtadi, R., Matsui, M., Arthur, T. S. & Hwang, S.-J. Magnesium borohydride: from hydrogen storage to magnesium battery. *Angew. Chem. Int. Ed.* **51**, 9780–9783 (2012).
16. Gregory, T. D., Hoffman, R. J. & Winterton, R. C. Nonaqueous electrochemistry of magnesium applications to energy storage. *J. Electrochem. Soc.* **137**, 775–780 (1990).
17. Connor, J. H., Reid, W. E. & Wood, G. B. Electrodeposition of metals from organic solutions. V. Electrodeposition of magnesium and magnesium alloys. *J. Electrochem. Soc.* **104**, 38–41 (1957).
18. Aurbach, D., Moshkovich, M., Schechter, A. & Turgeman, R. Magnesium deposition and dissolution processes in ethereal grignard salt solutions using simultaneous EQCM-EIS and in situ FTIR spectroscopy. *Electrochem. Solid. St.* **3**, 31–34 (2000).
19. Aurbach, D. et al. Progress in rechargeable magnesium battery technology. *Adv. Mater.* **19**, 4260–4267 (2007).
20. Chusid, O. et al. Solid-state rechargeable magnesium batteries. *Adv. Mater.* **15**, 627–630 (2003).
21. Ha, S.-Y. et al. Magnesium(II) bis(trifluoromethane sulfonyl) imide-based electrolytes with wide electrochemical windows for rechargeable magnesium batteries. *ACS Appl. Mater. Interf.* **6**, 4063–4073 (2014).
22. Gautam, G. S., Canepa, P., Richards, W. D., Malik, R. & Ceder, G. Role of structural H_2O in intercalation electrodes: the case of Mg in nanocrystalline xerogel-V_2O_5. *Nano Lett.* **16**, 2426–2431 (2016).
23. Yu, L. & Zhang, X. G. Electrochemical insertion of magnesium ions into V_2O_5 from aprotic electrolytes with varied water content. *J. Colloid Interface Sci.* **278**, 160–165 (2004).
24. Rahaman, M. S. A., Ismail, A. F. & Mustafa, A. A review of heat treatment on polyacrylonitrile fiber. *Polym. Degrad. Stab.* **92**, 1421–1432 (2007).
25. Piper, D. M. et al. Conformal coatings of cyclized-PAN for mechanically resilient si nano-composite anodes. *Adv. Energy Mater.* **3**, 697–702 (2013).
26. Son, S. B. et al. A stabilized PAN-FeS_2 cathode with an EC/DEC liquid electrolyte. *Adv. Energy Mater.* **4**, 1300961 (2014).
27. Pamula, E. & Rouxhet, P. G. Bulk and surface chemical functionalities of type IIIPAN-based carbon fibres. *Carbon* **41**, 1905–1915 (2003).
28. Wang, Z. X., Huang, B. Y., Xue, R. J., Huang, X. J. & Chen, L. Q. Spectroscopic investigation of interactions among components and ion transport mechanism in polyacrylonitrile based electrolytes. *Solid State Ion.* **121**, 141–156 (1999).
29. Bredas, J. L., Beljonne, D., Coropceanu, V. & Cornil, J. Charge-transfer and energy-transfer processes in π-conjugated oligomers and polymers: a molecular picture. *Chem. Rev.* **104**, 4971–5003 (2004).
30. Borodin, O., Zhuang, G. R. V., Ross, P. N. & Xu, K. Molecular dynamics simulations and experimental study of lithium ion transport in dilithium ethylene dicarbonate. *J. Phys. Chem. C.* **117**, 7433–7444 (2013).
31. Xu, K. Nonaqueous liquid electrolytes for lithium-based rechargeable batteries. *Chem. Rev.* **104**, 4303–4417 (2004).

32. Selim, R. & Bro, P. Some observations on rechargeable lithium electrodes in a propylene carbonate electrolyte. *J. Electrochem. Soc.* **121**, 1457–1459 (1974).
33. Shiga, T., Kato, Y., Inoue, M., Takahashi, N. & Hase, Y. Anode material associated with polymeric networking of triflate ions formed on Mg. *J. Phys. Chem. C* **119**, 3488–3494 (2015).
34. Xu, K. Electrolytes and interphases in Li-ion batteries and beyond. *Chem. Rev.* **114**, 11503–11618 (2014).
35. Dlubek, G., Brummer, O., Meyendorf, N., Dekhtyar, I. Y. & Fedchenko, R. G. Positron-annihilation studies on correction of structural crystal defects in plastically deformed PDFE alloys. *Phys. Status Solidi A* **42**, K15–K18 (1977).
36. Amin, R., Balaya, P. & Maier, J. Anisotropy of electronic and ionic transport in $LiFePO_4$ single crystals. *Electrochem. Solid St.* **10**, A13–A16 (2007).
37. Gershinsky, G., Yoo, H. D., Gofer, Y. & Aurbach, D. Electrochemical and spectroscopic analysis of Mg^{2+} intercalation into thin film electrodes of layered oxides: V_2O_5 and MoO_3. *Langmuir* **29**, 10964–10972 (2013).
38. Zhou, B., Shi, H., Cao, R. F., Zhang, X. D. & Jiang, Z. Y. Theoretical study on the initial stage of a magnesium battery based on a V_2O_5 cathode. *Phys. Chem. Chem. Phys.* **16**, 18578–18585 (2014).
39. Leger, C., Bach, S., Soudan, P. & Pereira-Ramos, J.-P. Structural and electrochemical properties of $\omega Li_xV_2O_5$ ($0.4 \leqslant x \leqslant 3$) as rechargeable cathodic material for lithium batteries. *J. Electrochem. Soc.* **152**, A236–A241 (2005).
40. Yue, Y. & Liang, H. Micro- and nano-structured vanadium pentoxide (V_2O_5) for electrodes of lithium-ion batteries. *Adv. Energy Mater.* **7**, 1602545 (2017).
41. Novák, P. & Desilvestro, J. Electrochemical insertion of magnesium in metal oxides and sulfides from aprotic electrolytes. *J. Electrochem. Soc.* **140**, 140–144 (1993).
42. Nam, K. W. et al. The high performance of crystal water containing manganese birnessite cathodes for magnesium batteries. *Nano Lett.* **15**, 4071–4079 (2015).
43. Sa, N. Y. et al. Is alpha-V_2O_5 a cathode material for Mg insertion batteries? *J. Power Sources* **323**, 44–50 (2016).
44. Lim, S.-C. et al. Unraveling the magnesium-ion intercalation mechanism in vanadium pentoxide in a wet organic electrolyte by structural determination. *Inorg. Chem.* **56**, 7668–7678 (2017).
45. Novák, P., Scheifele, W., Joho, F. & Haas, O. Electrochemical insertion of magnesium into hydrated vanadium bronzes. *J. Electrochem. Soc.* **142**, 2544–2550 (1995).
46. Novak, P., Imhof, R. & Haas, O. Magnesium insertion electrodes for rechargeable nonaqueous batteries: a competitive alternative to lithium? *Electrochim. Acta* **45**, 351–367 (1999).
47. Glushenkov, A. M. et al. Growth of V_2O_5 nanorods from ball-milled powders and their performance in cathodes and anodes of lithium-ion batteries. *J. Solid State Electr.* **14**, 1841–1846 (2010).

Acknowledgements

This work was supported by the Laboratory Directed Research and Development (LDRD) programme at the National Renewable Energy Laboratory (NREL). The authors greatly appreciate the constructive suggestions from H. Guthrey and D. H. Kim at NREL. The Alliance for Sustainable Energy, LLC (Alliance), is the manager and operator of NREL. Employees of the Alliance, under contract no. DE-AC36-08GO28308 with the US Department of Energy, authored this work.

Author contributions

S.-B.S. and C.B. developed the protocol for fabricating the Mg^{2+}-conducting interphase on Mg electrodes and performed electrochemical testing. C.B. supervised the work. K.X. synthesized APC electrolyte. T.G and C.W. contributed to the conductivity measurements. S.H. measured and analysed TOF-SIMS spectra of the Mg electrode. K.S. and A.C. measured and analysed XPS spectra of the Mg electrode. A.N. and A.S. performed FIB and STEM-EDS analysis. S.-B.S., C.B., K.X. and C.W. prepared the manuscript.

Competing interests

The authors declare no competing interests.

Additional information

Supplementary information is available for this paper at https://doi.org/10.1038/s41557-018-0019-6.

Reprints and permissions information is available at www.nature.com/reprints.

Correspondence and requests for materials should be addressed to C.B.

Publisher's note: Springer Nature remains neutral with regard to jurisdictional claims in published maps and institutional affiliations.